Drag and lift forces on random assemblies of wall-attached spheres in low-Reynolds-number shear flow

J. J. DERKSEN† AND R. A. LARSEN

Chemical and Materials Engineering, University of Alberta, Edmonton, Alberta, T6G 2G6, Canada

Direct numerical simulations of the shear flow over assemblies of uniformly sized, solid spheres attached to a flat wall have been performed using the lattice-Boltzmann method. The random sphere assemblies comprised monolayers, double layers and triple layers. The Reynolds number based on the sphere radius and the overall shear rate was much smaller than 1. The results were interpreted in terms of the drag force (the force in the streamwise direction) and lift force (the force in the wall-normal direction) experienced by the spheres as a function of the denseness of the bed and the depth of the spheres in the bed. The average drag and lift forces decay monotonically as a function of the surface coverage of the spheres in the top layer of the bed. The sphere-to-sphere variation of the drag and lift forces is significant due to interactions between spheres via the interstitial fluid flow.

Key words: particle/fluid flow, sediment transport

1. Introduction

In many engineered and naturally occurring situations, liquids or solid–liquid suspensions flow over beds of fine particles. The bed and the flow interact, and the nature and extent of the interactions depend on the flow characteristics, fluid properties and bed properties such as its density, topology, particle size (distribution) and inter-particle forces. In loose beds research questions revolve around (re)suspension of solids and sedimentation, the former due to erosion of the bed as a result of the fluid flow. In systems such as river and sea beds, and applications such as dredging, slurry pipelines and agitated slurry reactors, turbulence makes bed erosion a complicated, multi-scale process. The turbulent flow over the bed has a spectrum of length scales interacting with the bed. Once detached from the bed the suspended particles feel this multitude of flow scales that eventually determine if the particles get transported away from the bed or fall back into it again.

In this paper we zoom in on the hydrodynamic mechanisms responsible for detachment (i.e. erosion) of particle beds with a focus on the processes occurring at the small scale and consider fine particles. Fine being a relative qualification; here it means that the size of the particles is comparable to or smaller than the smallest flow length scales. As a result, the particles experience laminar flow. The

† Email address for correspondence: jos@ualberta.ca

beds considered are macroscopically flat which implies that the surface roughness of the beds is comparable to the size of the particles.

In the computational research described in this paper we build beds of equally sized spherical particles, supported by a flat wall; the particles in the bed are fixed, i.e. non-moving and non-rotating. The sphere configurations are randomly generated; inevitably, however, the denser beds show long-range order. Over the bed we generate a simple shear flow of Newtonian fluid and measure the force due to the flow on each individual sphere in the bed and decompose it into a drag force (in the streamwise direction) and a lift force (in the wall-normal direction). Analysis of the behaviour of drag and lift forces as a function of flow and bed conditions can be used in assessing the erosion capabilities of the flow. The research method described here is purely computational, i.e. we perform direct numerical simulations of the fluid flow over and inside the bed. The statistical properties (averages, root-mean-square values, probability distributions) of the forces as a function of the structure of the bed and the depth of the spheres in the bed are the main outcomes of this research.

There have been extensive – mostly theoretical – research efforts related to forces on single spheres in the proximity of walls, with an emphasis on the lift force. After Saffman's results (Saffman 1965, 1968) for lift on single spheres in free shear flows, Cox and co-workers (Vasseur & Cox 1976; Cox & Hsu 1977), and McLaughlin and co-workers (McLaughlin 1993; Cherakut & McLaughlin 1994; Cherakut, McLaughlin & Dandy 1999) reported on the effect walls have on the lift force. With the course of time these studies extended towards higher Reynolds numbers and closer wall proximities. Single spheres in direct contact with a wall have been studied by O'Neill (1968), Leighton & Acrivos (1985) and Krishnan & Leighton (1995). Detailed experiments have been reported by Mollinger & Nieuwstadt (1996) and King & Leighton (1997). Numerical work on lift on particles in the proximity of walls is, e.g. due to Patankar *et al.* (2001*a,b*) in two dimensions and (in three dimensions) due to Zeng, Balachandar & Fischer (2005) and Zeng *et al.* (2009).

In the context of hindered settling, fluidization and flow in porous media, hydrodynamic forces on assemblies of spherical particles have been studied by many researchers. The more recent works (Hill, Koch & Ladd 2001; Kandhai, Derksen & Van den Akker 2003; Van der Hoef, Beetstra & Kuipers 2005) employ computational experiments (direct numerical simulations) to probe the dependence of solids volume fraction, Reynolds number (Beetstra, Van der Hoef & Kuipers 2007), liquid rheology (Derksen 2009) and size or relative velocity distributions (Van der Hoef, Beetstra & Kuipers 2005; Yin & Sundaresan 2009) on the average drag force experienced by spherical particles in a dense suspension. The research presented in this paper is very much inspired by such computational approaches, now applied to sphere assemblies supported by walls.

The Reynolds number of the flow systems described here is defined as $Re = \dot{\gamma}_0 a^2 / \nu$, with $\dot{\gamma}_0$ being the overall shear rate over the bed (more precisely defined below), a the radius of the uniformly sized spheres and ν the kinematic viscosity of the fluid. In addition to the Reynolds number, the flow is defined by the spatial configuration of spheres, including their volume and surface fractions. We first study monolayers of spheres randomly placed on a flat wall. The independent variable of these simulations is the surface occupancy (or surface fraction) σ of the wall, i.e. $\sigma \equiv n\pi a^2$, with n being the number of spheres per unit surface area. We then make double layers of spheres by first making a dense bottom layer (typically having $\sigma = 0.70$) and then putting a less dense layer on top. Subsequently, we study triple layers. We limit the parameter space by only considering $Re \ll 1$, instigated by our interest in fine particles.

Results of the simulations comprise information regarding the drag and lift forces on the spheres in the fixed bed as a function of the bed configuration. We show that these hydrodynamic forces are strong functions of the (relative) placement of the spheres in the bed and that next to determining average force levels, the variability of the force (from sphere to sphere) needs to be considered.

The simulations presented are based on the lattice-Boltzmann (LB) method for simulating fluid flow (e.g. Succi 2001), with the spherical particle surfaces represented by an immersed boundary method (e.g. Goldstein, Handler & Sirovich 1993). In order to verify the computational approach we studied the effects of grid resolution and system size, the latter in terms of the impact the flow domain boundaries have on the hydrodynamic forces and also in terms of the number of spheres needed to reach converged statistical moments. We also compared simulations involving single spheres with the analytical, low-Reynolds-number solution for the force on a single sphere attached to a planar surface due to O'Neill (1968) and Leighton & Acrivos (1985). For $Re \ll 1$ the solution indicates that the lift force is much smaller (by a factor of order Re) than the drag force.

This paper is organized in the following manner. We start with defining our flow systems and the part of the parameter space we cover with our simulations. The numerical approach is sketched in the subsequent section. We then discuss verification tests – including the ones with a single sphere attached to a wall – that consider the level of resolution and domain size (relative to sphere size) and relate to accuracy and computational demand. Then we present our results for the drag and lift forces for a large number of sphere configurations (comprising monolayers, and double and triple layers). The paper, including its main conclusions, is summarized in the final section.

2. Flow systems

The basic flow configuration is sketched in figure 1: we have a flat wall of size $L \times W$ with spherical particles, each with radius a, randomly placed on it. All flow systems are periodic in the x (streamwise) and y (lateral) directions. We consider monolayers, double layers and triple layers. The monolayers are defined by a surface fraction σ_1. They are created by giving the non-overlapping spheres random centre locations (x_c, y_c) on the flat wall, i.e. they all have $z_c = a$. In order to achieve surface fractions $\sigma_1 > 0.35$, random placement on a surface needs to be followed by a compaction procedure, and then randomizing the system again by letting the spheres move granularly for some time, keeping the sphere centres at $z_c = a$. For typically $\sigma_1 \geqslant 0.5$, the monolayers show (long-range) order (see figure 2).

Double layers are built by first building a monolayer with $\sigma_1 = 0.70$ and all spheres at $z_c = a$. We then generate a second layer by randomly placing spheres at $z_c = 4a$. This layer has a surface fraction σ_2. We let fall this second layer (in the z-direction) on the first layer. In this process collisions between spheres are inelastic (restitution coefficient $e = 0.8$) and frictionless, and the spheres in the bottom layer are not allowed to move. After some time a static, double-layer bed has been created. The density of the bottom layer ($\sigma_1 = 0.70$) has been chosen such that particles in the second layer cannot fall through the bottom layer and thus do not touch the bottom wall; the minimum z-location of spheres in the second layer typically is $z_c = 2.0a$. Triple layers are build in a similar fashion, i.e. we first build (according to the procedure described above) a double-layer system with $\sigma_1 = \sigma_2 = 0.70$ and then drop the third layer with the surface fraction σ_3. A typical cross-section through a triple-layer bed is given in figure 2(d). All double-layer simulations presented here have the same bottom layer;
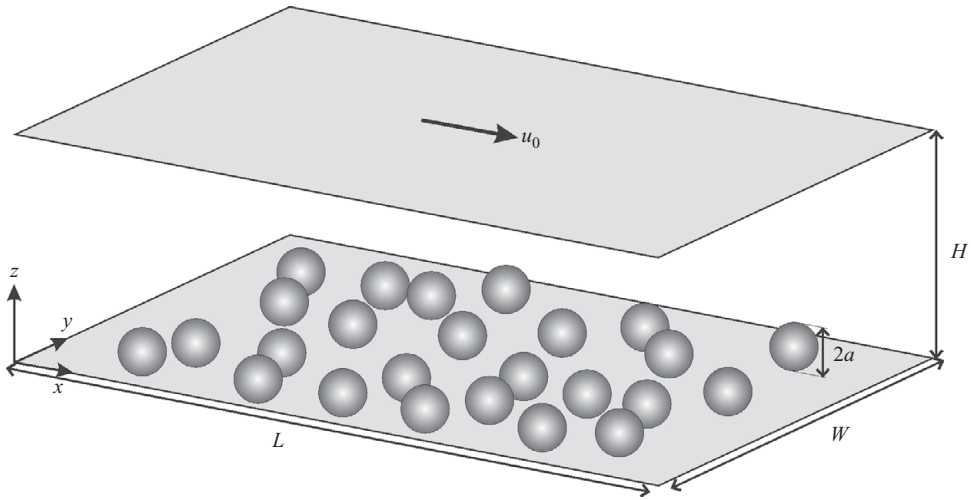
FIGURE 1. Flow geometry and coordinate system. Randomly placed spheres on the flat bottom wall experience a shear flow due to the motion in the x-direction of an upper wall.
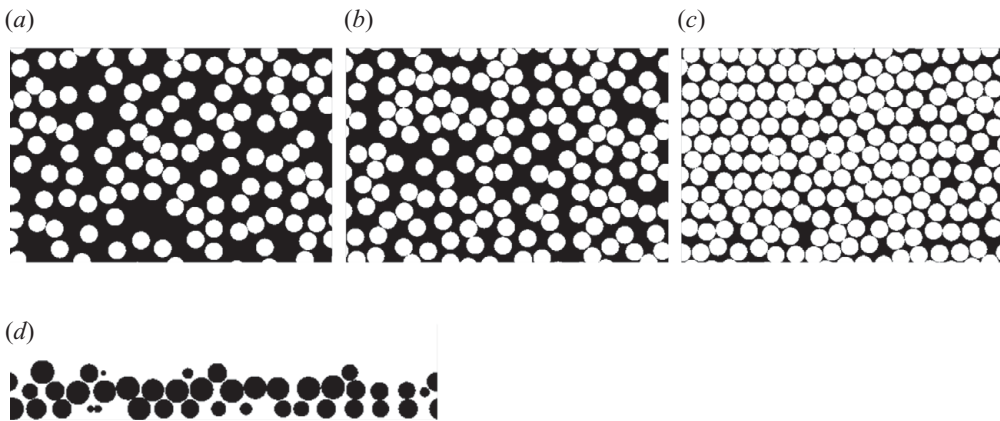
(*a*)   (*b*)   (*c*)

(*d*)

FIGURE 2. Top view of monolayers: (*a*) $\sigma_1 = 0.4$, (*b*) $\sigma_1 = 0.5$, (*c*) $\sigma_1 = 0.7$. (*d*) Cross-section (xz-plane) through a triple-layer bed with $\sigma_1 = \sigma_2 = 0.7$ and $\sigma_3 = 0.4$.

all triple-layer simulations have the same two lower layers. The lower layers are dense so that each sphere in the bed can be associated with a specific layer.

Above the beds of spheres a shear flow is created by placing a wall parallel to the bottom wall at a distance H and giving that wall a velocity u_0 in the positive x-direction (see figure 1). The overall shear rate $\dot{\gamma}_0$ as, e.g. used in $Re = \dot{\gamma}_0 a^2/\nu$ for monolayers is defined as $\dot{\gamma}_0 \equiv u_0/H$, for double and triple layers it is $\dot{\gamma}_0 = u_0/(H - 2a)$ and $\dot{\gamma}_0 = u_0/(H - 4a)$ respectively; the definition of $\dot{\gamma}_0$ depends on the number of layers in order to account for the reduced open space above the bed as a result of the presence of sphere layer(s). Later in this paper, we will see that the shear rates actually experienced by the beds slightly differ from $\dot{\gamma}_0$. The placement of the moving wall (in terms of the aspect ratio H/a) has an influence on the hydrodynamic forces acting on the spheres. This sensitivity has been investigated and H/a has been chosen such that its impact on the forces is small. If we compare cases with different numbers of layers, H is increased by an amount $2a$ for each additional layer of spheres. During the flow simulations the spheres are immobile.

3. Modelling approach

As in many of the earlier works on the subject of drag on sphere assemblies, we used the LB method (Chen & Doolen 1998; Succi 2001) to solve for the flow of interstitial liquid. The method has a uniform, cubic grid (grid spacing Δ) on which fictitious fluid particles move in a specific set of directions and collide to mimic the behaviour of an incompressible, viscous fluid. The specific LB scheme employed here is due to Somers (1993); see also Eggels & Somers (1995). The no-slip condition at the spheres' surfaces was dealt with by means of an immersed boundary (or forcing) method (Goldstein *et al.* 1993; Derksen & Van den Akker 1999). In this method, the sphere surface is defined as a set of closely spaced points (the typical spacing between points is 0.7Δ), not coinciding with grid points. At these points the (interpolated) fluid is forced to zero-velocity according to a control algorithm. Adding up (discrete integration) of the forces needed to maintain no-slip provides us with the (opposite; action is minus reaction) force the fluid exerts on the spherical particle. In this procedure we generally do not distinguish normal (pressure-related) and shear forces. We have validated and subsequently used this method extensively to study the interaction of (static as well as moving) solid particles and Newtonian and non-Newtonian fluids (Ten Cate *et al.* 2004; Derksen & Sundaresan 2007; Derksen 2008, 2009). For instance, simulation results of a single sphere sedimenting in a closed container were compared with PIV experiments of the same system and showed good agreement in terms of the sphere's trajectory, as well as the flow field induced by the motion of the falling sphere (Ten Cate *et al.* 2002). For dense suspensions (with solids volume fractions up to 0.53) Derksen & Sundaresan (2007) were able to quantitatively correctly represent the onset and propagation of instabilities (planar waves and two-dimensional voids) of liquid–solid fluidization as experimentally observed by Duru *et al.* (2002) and Duru & Guazelli (2002).

It should be noted that having a spherical particle on a cubic grid requires a calibration step, as earlier realized by Ladd (1994). He introduced the concept of a hydrodynamic radius. The calibration involves placing a sphere with a given radius a_g in a fully periodic cubic domain in creeping flow and (computationally) measuring its drag force. The hydrodynamic radius a of that sphere is the radius for which the measured drag force corresponds to the expression for the drag force on a simple cubic array of spheres due to Sangani & Acrivos (1982) which is a modification of the analytical expression due to Hasimoto (1959). Usually a is slightly bigger than a_g, with $a - a_g$ typically equal to half a lattice spacing or less. In the present work, given radii a_g are selected such that the resulting hydrodynamic radius gets a round number: $a = 6.0$, 8.0 or 12.0. The default radius is $a = 6.0$. Simulations with the larger radii were conducted to quantify grid effects.

The simulations were started by setting the upper wall in motion above a zero-velocity liquid layer. It then approximately takes a time span $t \sim H^2/\nu$ for the flow system to reach the steady state. In a typical simulation this corresponds to 5×10^4 time steps. After the steady state has been reached, we analyse the results, mostly in terms of drag and lift forces exerted by the flow on the spheres.

4. Results

4.1. *Single-sphere validations*

For validation of the numerical procedure, and for checking the effects of spatial resolution and domain size ($L \times W \times H$, see figure 1) relative to sphere size, first a single sphere was placed on the bottom wall in the flow domain. For the flow around

a single solid, immobilized sphere attached to a flat wall in further unbounded simple shear flow, an analytical solution in the Stokes flow limit – including an expression for the drag force acting on the sphere – has been presented by O'Neill (1968). Leighton & Acrivos (1985) extended the analysis to account for inertial effects so that the lift force could be determined. For situations with $Re = \dot{\gamma}_0 a^2/\nu \ll 1$, the drag and lift force expressions read $F_D = 32.1\mu\dot{\gamma}_0 a^2$ and $F_L = 9.22 Re\mu\dot{\gamma}_0 a^2$ respectively (with $\mu = \nu\rho$ the dynamic viscosity). Inspired by these expressions, we define dimensionless drag and lift forces as $F_D^* \equiv F_D/\mu\dot{\gamma}_0 a^2$ and $F_L^* \equiv F_L/Re\mu\dot{\gamma}_0 a^2$ respectively. The force on the sphere in the x-direction is the drag force and the force in the z-direction (in terms of the coordinate system as defined in figure 1) is the lift force. It should be noted that if the sphere is allowed to move (e.g. rolling along the wall at some very small finite separation distance), the lift force would be substantially reduced (Krishnan & Leighton 1995).

In the base-case simulation the grid had a resolution such that $a = 6.0$, and $L = 36a$, $W = 24a$, $H = 12a$ and $Re = 0.05$. For the base-case simulation we find $F_D^* = 32.3 \pm 0.05$ and $F_L^* = 7.9 \pm 0.6$. The uncertainties (the number after $\pm$ indicates two standard deviations) relate to the placement of the sphere relative to the grid. Due to discretization (of the flow domain and of the surface of the sphere) the forces slightly change if the sphere is displaced with respect to the grid. Given the periodic conditions, displacing the sphere by an integer number of lattice spacings in the x- or y-direction has no effect. Its large standard deviation indicates that the lift force is relatively sensitive to this effect. It should be noted, however, that for the base-case conditions the lift force is much weaker than the drag force: the ratio of the drag force over the lift force is approximately $F_D/F_L \approx 80$.

If we increase the flow domain in the x- and/or y-direction (i.e. increase L and/or W), the drag and lift forces do not change much: for $L = 72a$ and the rest base-case conditions the drag force increased by 0.4 % and lift increased by 0.7 %; for $W = 36a$ (and further base-case conditions) the lift force went up 0.1 % while the drag force virtually stayed the same. It should be noted that the relative change in the drag and lift forces due to changes in L and W has been studied for one specific sphere placement (relative to the grid) only.

The sensitivity with respect to the domain height H is somewhat stronger as we show in figure 3. The drag force decreases and the lift force increases if H is made larger. For the drag force we reach good agreement with the O'Neill (1968) result of $F_D^* = 32.1$ (the value for F_D^* at $H/a = 24$ is 32.1 ± 0.05). On the one hand this is surprising given the modest spatial resolution of $a = 6.0$; on the other hand, it is not given the fact that we calibrated the hydrodynamic radius based on the drag force (albeit under different geometrical and flow conditions). The simulated lift force is lower (by some 8 % for $H/a = 24$) than the analytical result of $F_L^* = 9.22$. The influence of the Reynolds number was investigated for the specific situation of the sphere centre having an x- and a y-location coinciding with the x- and y-locations of lattice nodes, see the results in figure 4. For $Re \leqslant 0.05$, the dimensionless drag force is practically Reynolds-independent. The dimensionless lift converges in a somewhat erratic manner to a value of approximately 8.6 for $Re \leqslant 0.01$. The convergence of F_L^* to a constant value for low Re ($Re \leqslant 0.01$) agrees with the analytical result of Leighton & Acrivos (1985). The decrease of F_L^* with increasing Reynolds number (figure 4) indicates that for a higher Reynolds number ($Re > 0.01$) the dependence of the lift force on the sphere radius is weaker than a^4, in accordance with the observations (and the literature data cited) by Zeng *et al.* (2009).

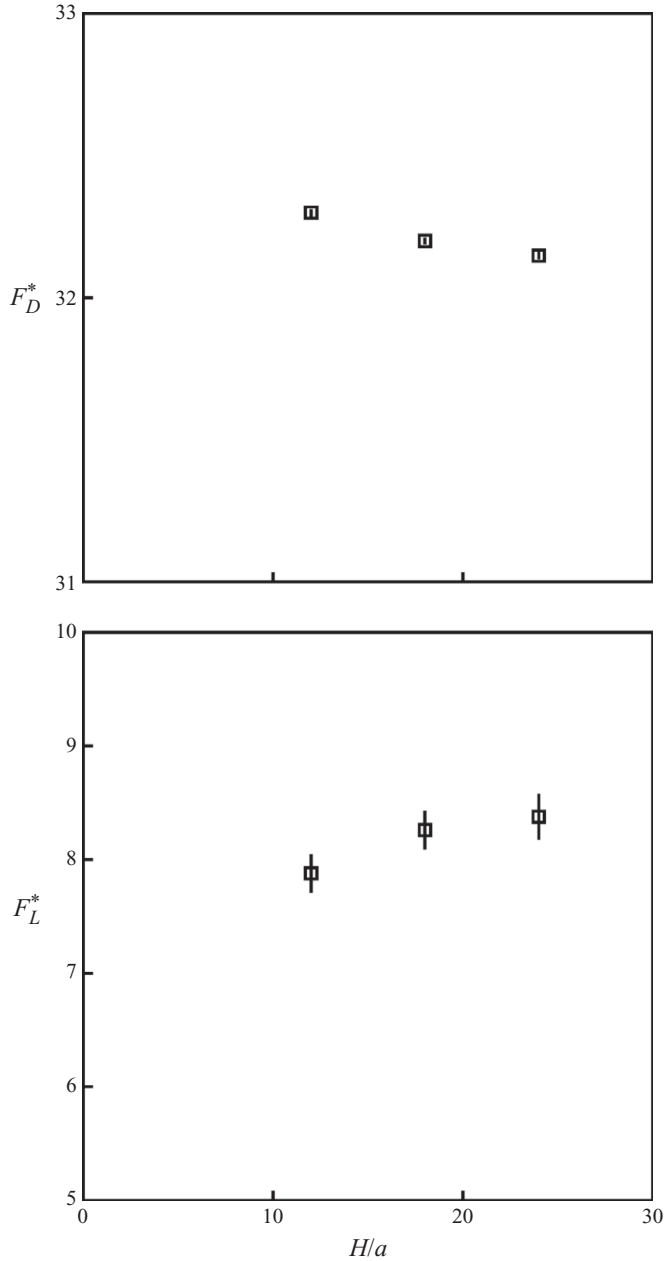FIGURE 3. Dimensionless drag F_D^* and lift F_L^* forces as a function of the system height H with (except for H) base-case conditions (as defined in the text). The error bars have a total length of two times the standard deviation (one on either side). Each data point represents the average and standard deviation of six placements of the sphere centre relative to the grid.

The combined effect of Re and H/a on the drag and the lift force was investigated by performing a set of six simulations (each with a different placement of the sphere relative to the grid) at $Re = 0.01$ (smaller than in the base case) and $H/a = 24$ (larger than in the base case) that resulted in $F_D^* = 32.1 \pm 0.05$ and $F_L^* = 9.1 \pm 0.6$. The
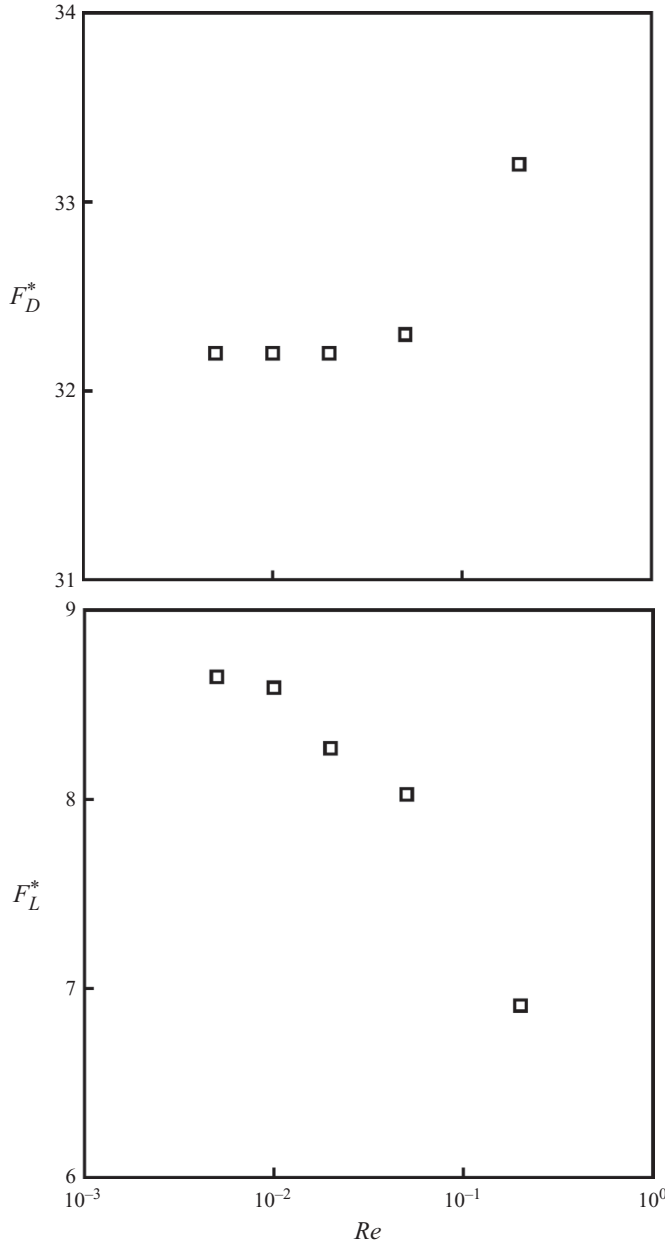
FIGURE 4. Dimensionless drag F_D^* and lift F_L^* forces as a function of the Reynolds number with (except for Re) base-case conditions (as defined in the text). Results for a single-sphere placement (relative to the grid).

analytical expressions (O'Neill 1968; Leighton & Acrivos 1985) are within the error margin of these simulations.

A grid refinement study for a single-sphere placement (relative to the grid) under base-case conditions ($H/a = 12$ and $Re = 0.05$, see figure 5) shows that refining the grid has a less than 0.5 % effect on the drag force. The dimensionless lift force, however, reduces by 3.5 % if the grid spacing is reduced from $a/6$ to $a/12$.
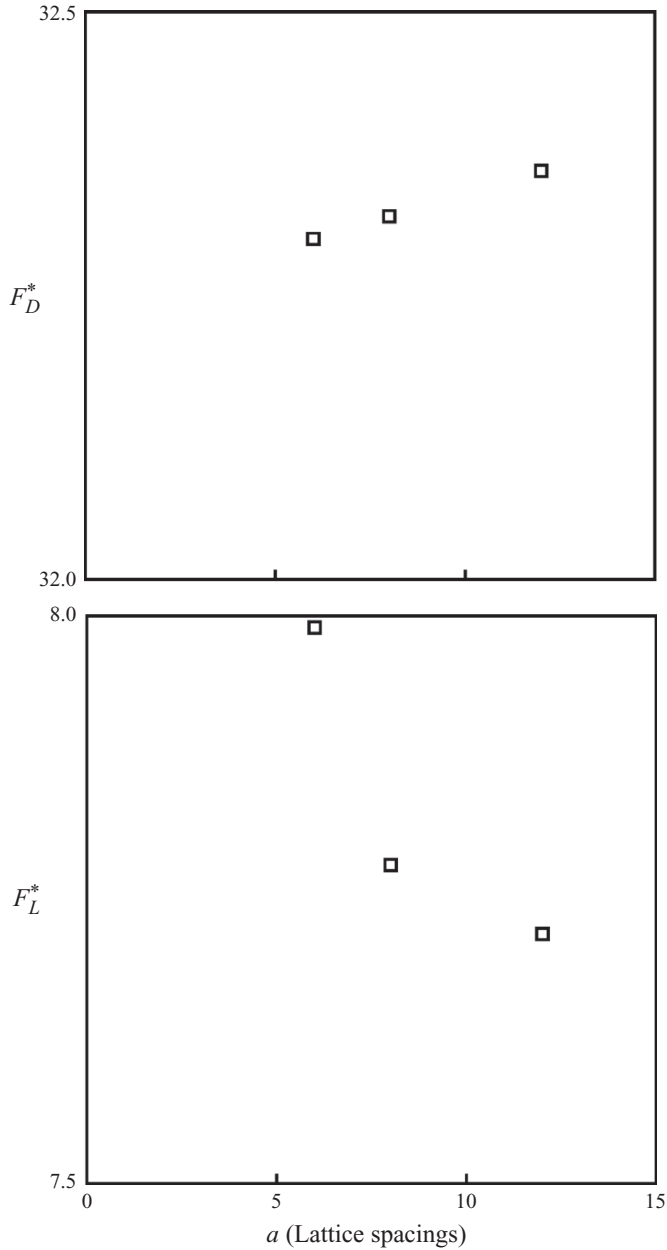
FIGURE 5. Dimensionless drag F_D^* and lift F_L^* forces as a function of the spatial resolution as expressed in the number of lattice spacings per sphere radius a. Base-case conditions. Results for a single-sphere placement (relative to the grid).

The conclusion of this single-sphere study is that the drag of a wall-bounded sphere in slow (low Re) shear flow can be well represented (within some 1 % of the analytical result) by our numerical procedure that (it should be noted again) has been calibrated. The lift force is predicted less accurately and is relatively sensitive to the placement of the sphere in the grid. Compared to the drag force, the lift force depends stronger on the wall-normal domain size, the Reynolds number and the spatial resolution of the

simulations. For $Re \leqslant 0.01$, $H/a \geqslant 24$ and $a = 6$, the uncertainty interval of simulated lift forces covers the analytical result, the centre of the interval being 1.5 % off. The grid refinement results (done for the base case, and for reasons of computational affordability for only one placement of the sphere in the grid) indicate a somewhat larger deviation. The error in the simulated average lift force is estimated to be 4 % (still smaller than the uncertainty margins – two standard deviations – due to sphere placement in the grid of 6 %). It should be noted, however, that the simulations tend to underestimate lift.

For the practical purpose of studying erosion of fine particle beds, the lift force being not as accurate as the drag force is not a critical issue. For low Reynolds numbers, the drag force is much stronger than the lift force. The single-sphere results also provided indications as to when the dimensionless drag force F_D^* and lift force F_L^* tend to become independent of the flow domain size (relative to sphere size) and Reynolds number, which is important information when setting up and interpreting many-sphere simulations.

4.2. *Monolayers of spheres*

We now turn to situations where the bottom plate is partially covered with spheres that all rest on the plate, i.e. their z-centre locations are $z_c = a$. The specific physical situation with the surface coverage fraction $\sigma_1 = 0.25$ and $Re = 0.05$ has been studied with respect to its sensitivity to numerical (e.g. resolution) and semi-numerical (e.g. domain size) settings. This situation and the verifications are discussed first.

Figure 6 gives an impression of the flow field in terms of the fluid velocity in between and closely above the spheres (note that the computational domain extends to $z = 12a$, i.e. much further than displayed in figure 6(*b*)). It can be seen that the shear flow only partially penetrates the space between the spheres which obviously has consequences for the hydrodynamic forces acting on the spheres. Compared to the single-sphere values of $F_D^* \approx 30$ and $F_L^* \approx 9$, the average drag and lift forces per sphere for the monolayer with $\sigma_1 = 0.25$ reduce drastically; see the results in figure 7 that indicate the values of the order of 10 and 1 for dimensionless drag and lift forces respectively. In figure 7 the effect of the horizontal system size has been investigated. The three data points per panel relate to $L \times W$ equal to $24a \times 16a$, $36a \times 24a$ and $48a \times 32a$. The standard deviations as indicated in the figure are the result of different (random) sphere configurations; they get smaller when the flow systems get larger. Most of the subsequent simulations were done for systems with $L \times W = 36a \times 24a$ as a compromise between small standard deviation and computational effort.

As for the single-sphere simulations, the effect of the spatial resolution on hydrodynamic forces was tested by comparing simulations with $a = 6.0$, 8.0 and 12.0. This was done for one random sphere configuration and flow conditions as defined in table 1. The results for the average drag and lift forces show good agreement between the grids; the drag force is virtually grid-independent, and the lift forces are within a 3 % margin.

A subtle issue comes up when comparing different vertical domain sizes. Again one sphere configuration was considered, and H was increased from $12a$ (the default size) to $18a$, $24a$ and $36a$ while keeping the Reynolds number constant. Dimensionless drag and lift forces then show a systematic decline, see figure 8. Closer inspection demonstrates that this decline can be almost fully attributed to the way the drag and lift forces have been scaled ($F_D^* \equiv F_D/\mu\dot{\gamma}_0 a^2$ and $F_L^* \equiv F_L/Re\mu\dot{\gamma}_0 a^2 = F_L/\rho\dot{\gamma}_0^2 a^4$ with $\dot{\gamma}_0 \equiv u_0/H$). As is clear from figure 6, however, the shear flow does not fully

Resolution of a (lattice spacings)	F_D^*	F_L^*
6	13.30	1.539
8	13.30	1.497
12	13.29	1.511

TABLE 1. Simulations with different spatial resolution and $\sigma_1 = 0.25$, $L = 36a$, $W = 24a$, $H = 12a$, $Re = 0.05$.
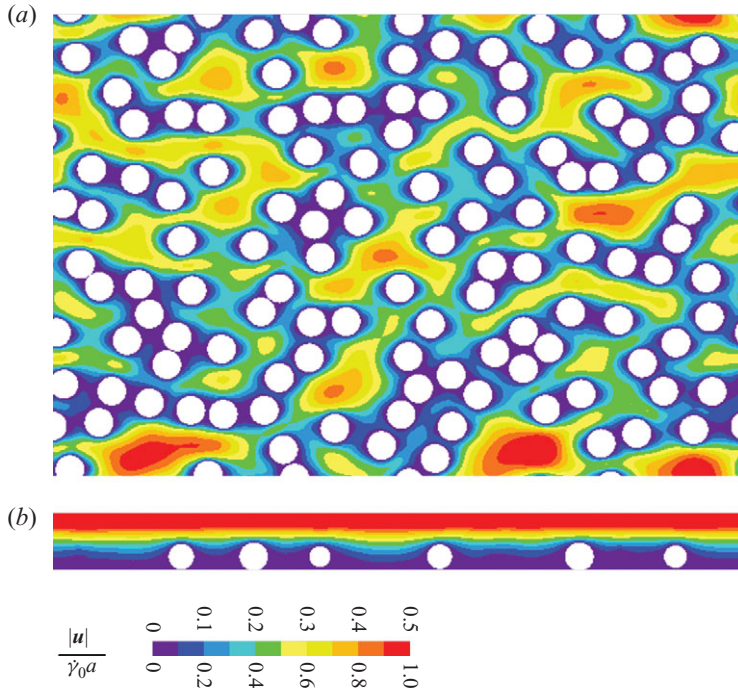

FIGURE 6. Absolute velocity in (a) horizontal (xy) plane at $z = a$ and (b) in a vertical streamwise (xz) plane. The top colour scale relates to (a) and the bottom scale to (b). $\sigma_1 = 0.25$ and $Re = 0.05$.

penetrate the particle layer so that u_0/H may not be a good measure for the shear rate experienced by the spheres in the monolayer. Also, the extent to which the shear rate experienced by the bed deviates from u_0/H depends on H (relative to a). This is illustrated in figure 9 where we show profiles of the streamwise superficial fluid velocity as a function of z for different vertical system sizes. These profiles are similar to the ones measured by Mouilleron, Charru & Eiff (2009) inside granular beds moved by a shear flow at Shields numbers not much above the critical value at which the onset of particle motion occurs and particle-based Reynolds numbers are smaller than 1.

The observations in figure 9 allow us to define a more representative measure for the shear rate (symbol $\dot{\gamma}_b$) felt by the spheres as the slope of the straight portion of the velocity profile. If we use this shear rate for normalization, i.e. change the definitions to $F_D^* = F_D/\mu\dot{\gamma}_b a^2$ and $F_L^* = F_L/\rho\dot{\gamma}_b^2 a^4$, the dependences with respect to H/a virtually disappear (see the closed symbols in figure 8). From this moment on,

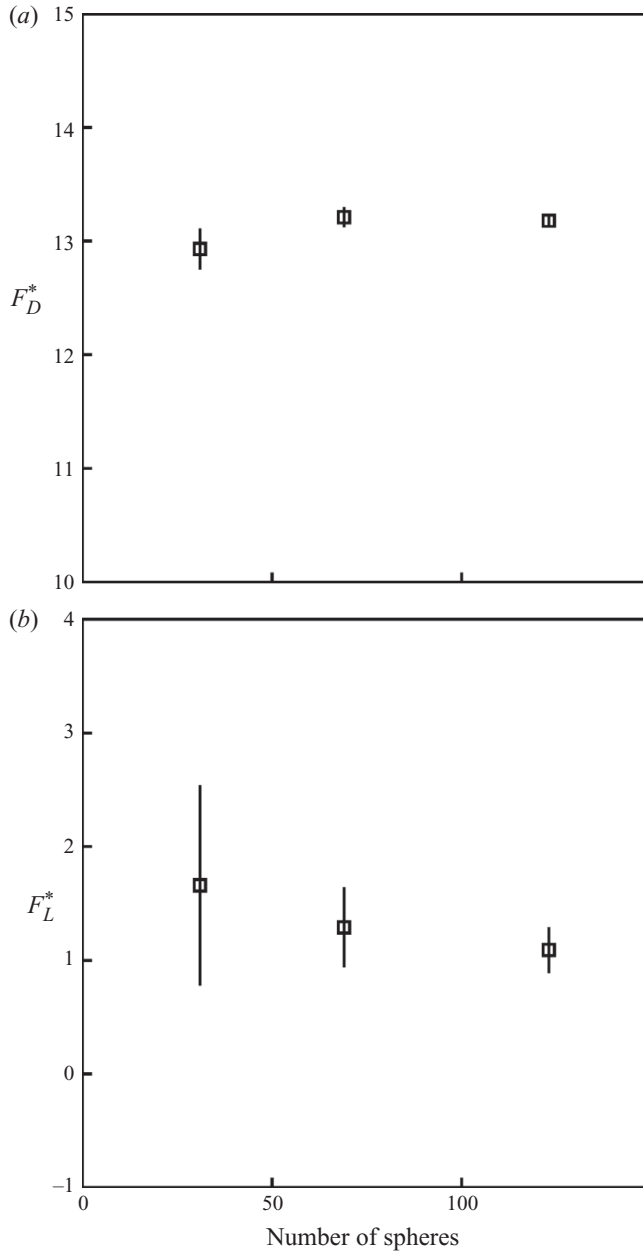(*a*) 15

F_D^*

(*b*) 4

F_L^*

Number of spheres

FIGURE 7. Average drag (*a*) and lift (*b*) forces in a monolayer as a function of the horizontal system size (expressed as the number of spheres in the monolayer). The total length of each error bar is two times the standard deviation of the average force based on five monolayer realizations. $H = 12a$, $\sigma_1 = 0.25$ and $Re = 0.05$.

the dimensionless drag and lift force results will be based on normalizations using $\dot{\gamma}_b$. Note that we do not change the Reynolds number definition. It is still based on $\dot{\gamma}_0$ (i.e. Re is fully determined by the input parameters). The rationale for this is that we wish Re to be fully determined by input parameters ($\dot{\gamma}_0$, a and ν). For the simulations reported in this paper, Re would at most increase by 8 % (0.054 instead of 0.05 under
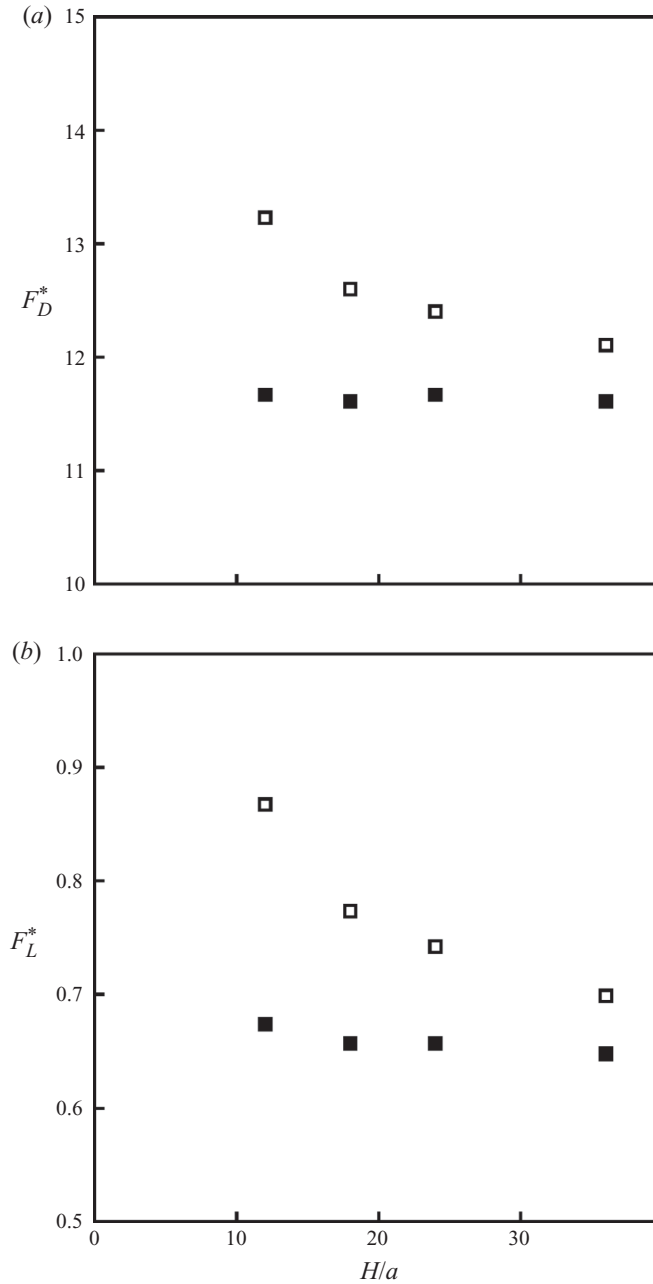
FIGURE 8. Average drag (*a*) and lift (*b*) forces in a monolayer as a function of the vertical system size *H*. Results for a single monolayer configuration. The open symbols relate to force normalization based on $\dot{\gamma}_0 = u_0/H$ and the closed symbols to a normalization based on $\dot{\gamma}_b$ (see the text and figure 9). $L = 48a$, $W = 32a$, $\sigma_1 = 0.25$ and $Re = 0.05$.

the base-case condition) if we base it on $\dot{\gamma}_b$ and the precise value of Re is not that critical (as long as $Re \ll 1$).

Given the above assessments and insights we now use an $L \times W \times H = 36a \times 24a \times 12a$ domain with spheres of radius $a = 6.0$ lying on the bottom
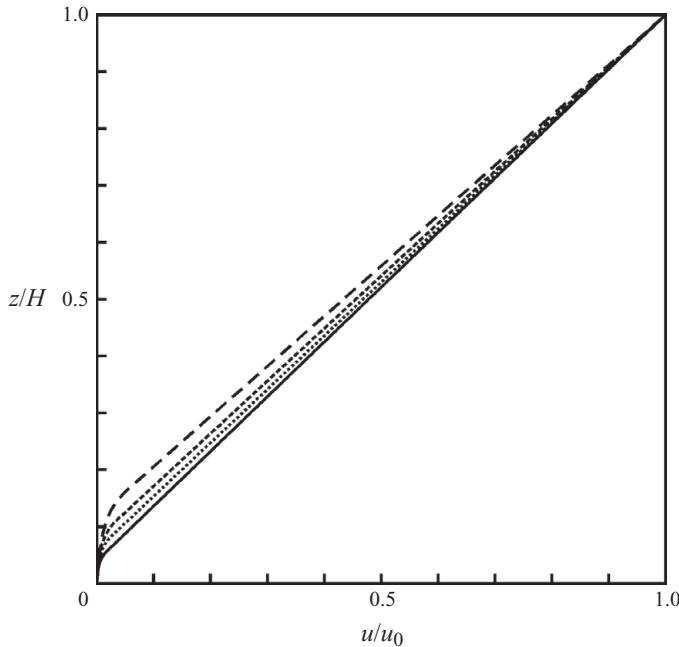
FIGURE 9. Average superficial x-velocity profile over and in a monolayer. Comparison between different vertical system sizes: $H = 12a$ (long dash), $H = 18a$ (short dash), $H = 24a$ (dotted) and $H = 36a$ (solid). The slope of the straight portion of each curve is recognized as $\dot{\gamma}_b$. $L = 48a$, $W = 32a$, $\sigma_1 = 0.25$ and $Re = 0.05$.

wall and a shear flow with $Re = 0.05$ to study the dependence of the average drag and lift forces experienced by the spheres on the surface occupancy σ_1. Figure 10 summarizes the main results. Each data point in figure 10 represents at least five simulations, i.e. five different random sphere configurations experiencing the same overall shear flow. The error bars indicate the standard deviation of the *average* lift and drag forces. Both the average drag force and the average lift force decrease strongly with increasing sphere density on the bottom plate. This is the result of the shear flow penetrating less deep in the monolayer as it gets denser. This effect is quantified in figure 11. There we show how the intercept of the extrapolated linear shear field above the bed with the z-axis (symbol p, see the inset of figure 11) depends on σ_1. The denser the monolayer, the more the flow skims over the monolayer, thereby reducing the average drag and lift forces.

To see how much the forces experienced by the individual spheres deviate from the average force, the variability of the forces is displayed in figure 12 in terms of the root-mean-square (r.m.s.) values of the deviation of the drag and lift forces from their average values (r.m.s.(F_D^*) and r.m.s.(F_L^*) respectively). Especially for the lift force these results are intriguing. In the first place r.m.s.(F_L^*) is larger than the average dimensionless lift force over the entire σ_1 range considered, in the second place r.m.s.(F_L^*) can get significantly larger than the single-sphere value of 9.22 and in the third place r.m.s.(F_L^*) goes through a maximum at around $\sigma_1 = 0.06$. At $\sigma_1 = 0.06$ the average centre-to-centre spacing of the spheres is approximately 3.6 times the sphere diameter.

For very low values of σ_1 the spheres do not interact hydrodynamically and all spheres would feel the same single-sphere lift force and there would be no sphere-to-sphere variability; thus, r.m.s.(F_L^*) would approach zero. For denser systems the
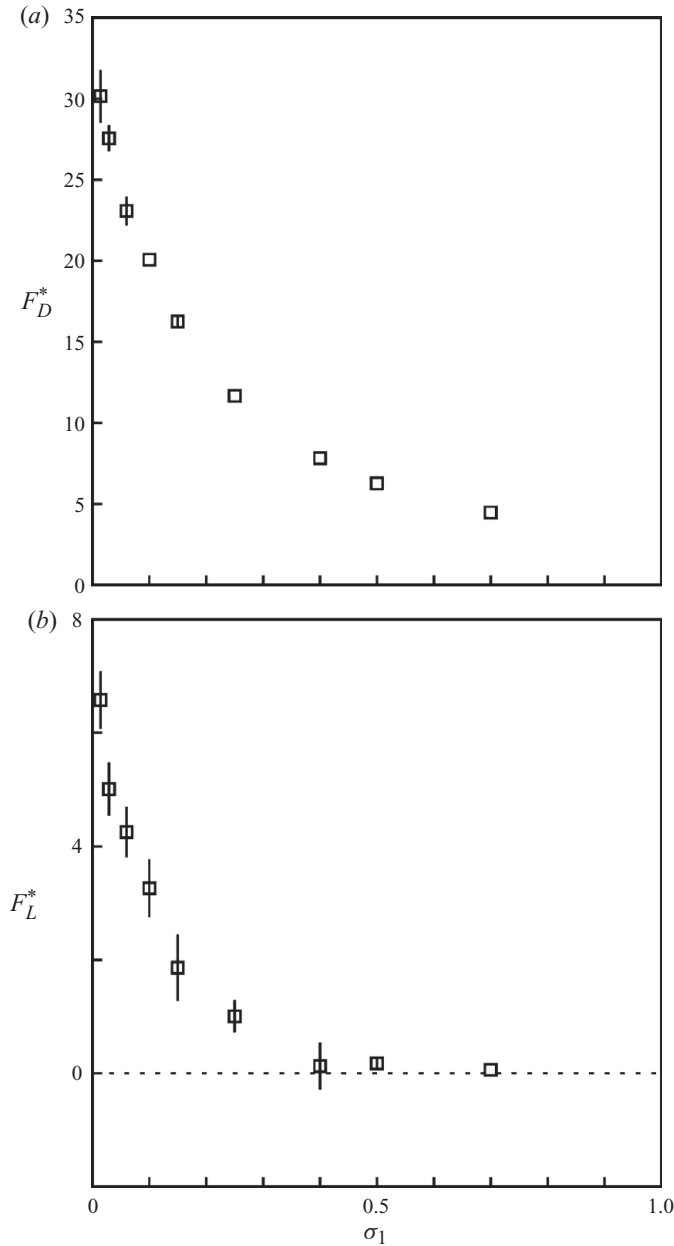
FIGURE 10. Dimensionless drag (*a*) and lift (*b*) forces as a function of the surface occupancy σ_1 in a monolayer. The total length of the error bars is two times the standard deviation of the average forces. If the bars are smaller than the symbol, then they would not be displayed. $H = 12a$, $L = 48a$, $W = 32a$ and $Re = 0.05$.

spheres start feeling one another, i.e. the flow field around one sphere impacts the surrounding spheres and vice versa. The three-dimensional flow experienced by each sphere as a result of the surrounding spheres strongly and erratically induces forces in the vertical (negative and positive) direction. These vertical forces are not necessarily inertial lift forces (in the Saffman sense); they contain contributions of viscous drag as a result of vertical components of the flow about the sphere induced
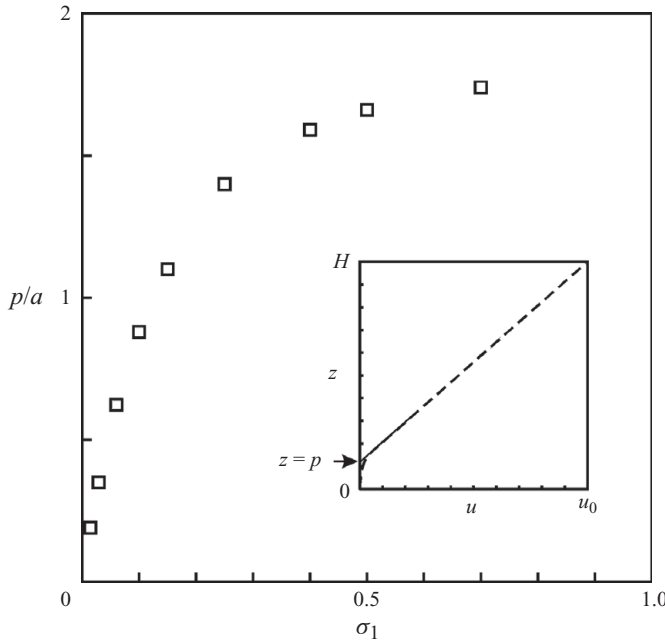
FIGURE 11. Intercept of the linear part of the velocity profile with the ordinate (symbol p as defined in the inset) as a function of σ_1 for monolayers. $H = 12a$, $L = 48a$, $W = 32a$ and $Re = 0.05$.

by other spheres surrounding it. Since at low Reynolds numbers the drag force is much stronger than the lift force (Leighton & Acrivos 1985), the vertical viscous drag forces can easily exceed the single-sphere inertial lift force. For still denser systems (beyond $\sigma_1 = 0.06$ according to figure 12) r.m.s.(F_L^*) gets smaller for the same reason the average lift force gets smaller, i.e. because the shear flow is less able to penetrate the monolayer, thus weakening the forces on the spheres. The inset in figure 12 shows the probability density functions (p.d.fs) of the lift force when its variability goes through its maximum (at $\sigma_1 = 0.06$) and (for comparison) at $\sigma_1 = 0.25$. At $\sigma_1 = 0.06$ some individual spheres feel vertical forces as large as $50\rho\dot{\gamma}_b^2 a^4$, i.e. more than five times the single-sphere inertial lift force.

The variability of the drag force (in terms of r.m.s.(F_D^*)) goes through a similar dependence on σ_1 as r.m.s.(F_L^*), but in a dimensionless sense is approximately a factor of 6 weaker. Given $Re = 0.05$ in the simulations considered here, the ratio r.m.s.(F_D)/r.m.s.(F_L) (i.e. the ratio of dimensional drag and lift forces variability) therefore is $1/6Re \approx 3$.

To further investigate the lift force variability and its interpretation as a viscous drag force due to a vertical fluid flow, the behaviour of the vertical (z) fluid velocity component in the monolayer was studied in more detail. In figure 13 $u_z^* \equiv u_z/\dot{\gamma}_0 a$ is shown at the $z = a$ level in terms of contour plots. The presence of spheres on the surface clearly induces vertical velocities; the structure and amplitude of the vertical velocity field depend on the surface occupancy. This is further detailed in figure 14 (a), which shows the r.m.s. levels r.m.s.(u_z^*) of the vertical velocity (with average u_z^* being zero) of the fluid at $z = a$ in a monolayer as a function of σ_1. The form of this dependence shows similarity with the way r.m.s.(F_L^*) depends on σ_1 (figure 12), although the similarity is not perfect (the maximum for r.m.s.(F_L^*)
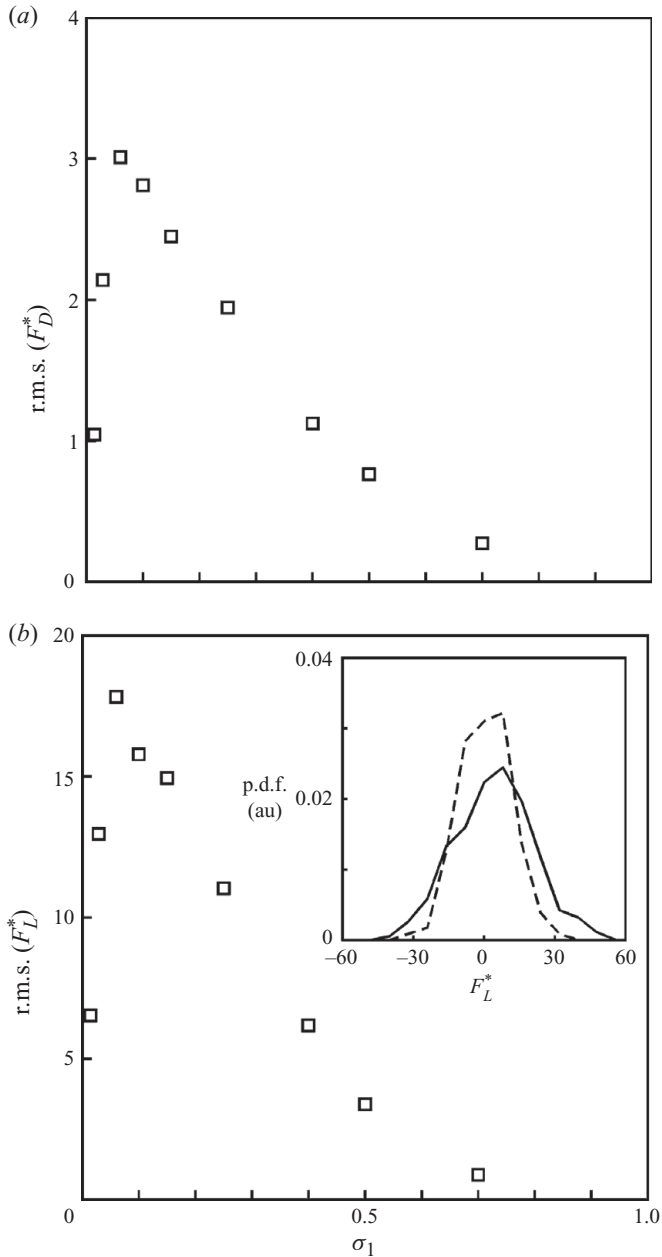
(*a*)

(*b*)

FIGURE 12. Root-mean-square values of drag (*a*) and lift (*b*) forces as a function of σ_1 for monolayers. The inset in (*b*) shows the p.d.f. of the lift force for $\sigma_1 = 0.06$ (solid curve) and 0.25 (dashed curve). For all data points: $H = 12a$ and $Re = 0.05$.

is reached at/near $\sigma_1 = 0.06$, and that for r.m.s.(u_z^*) at/near $\sigma_1 = 0.1$). If we plot r.m.s.(F_L^*) against r.m.s.(u_z^*), as is done in figure 14(*b*), an approximately linear relationship can be identified with an estimated proportionality constant $\beta \approx 550$ (defined by r.m.s.$(F_L^*) = \beta \cdot$ r.m.s.(u_z^*)). In a (overly) simple conjecture, we make the vertical force variability proportional to the vertical velocity variability with proportionality constant $6\pi a\mu$ (as in Stokes drag). In a dimensionless form this would imply r.m.s.$(F_L^*) = 6\pi/Re \cdot$ r.m.s.(u_z^*). With $Re = 0.05$ (as in the simulations that
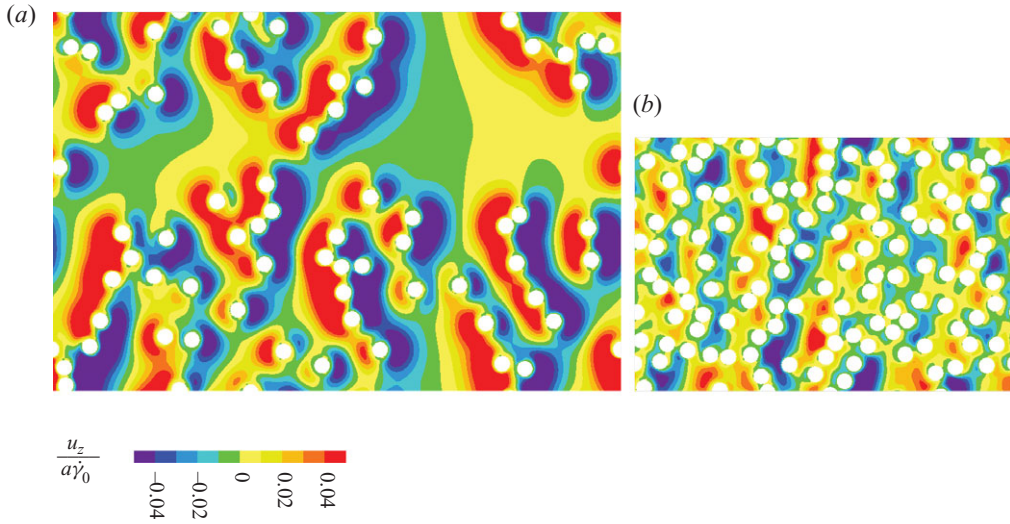
FIGURE 13. Vertical (z) velocity in a monolayer at $z = a$ with (a) $\sigma_1 = 0.06$ and (b) $\sigma_1 = 0.25$ and $Re = 0.05$.
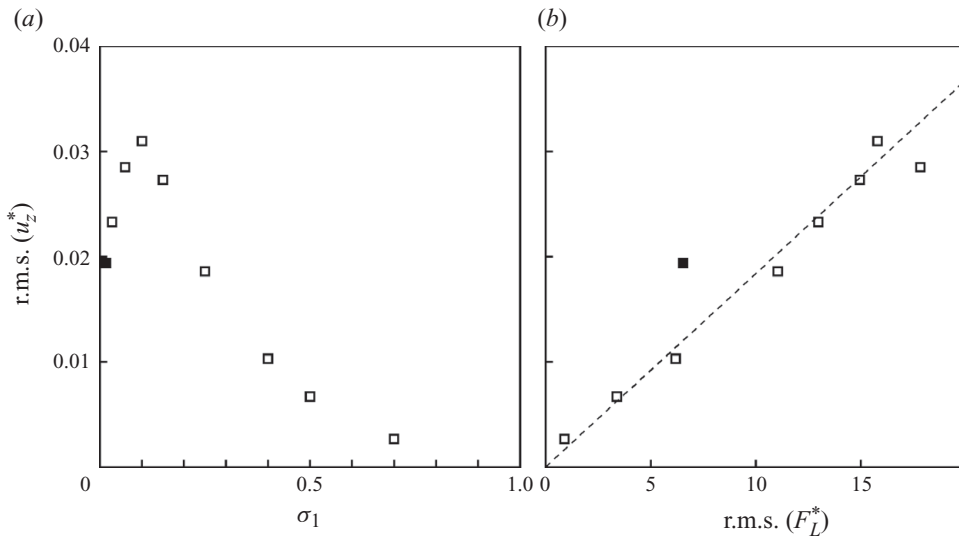

FIGURE 14. (a) Root-mean-square values of the vertical velocity component u_z at $z = a$ as a function of σ_1 for monolayers. (b) r.m.s.(F_L^*) (data from figure 12) versus r.m.s.(u_z^*); dashed line: linear fit discarding the filled-square data point which corresponds to the filled square in (a). The inverse slope of the straight line amounts to $\beta = 550$. For all data points: $H = 12a$ and $Re = 0.05$.

generated figures 12 and 14), $6\pi/Re \approx 380$, which is of the same order of magnitude as the fitted value of β. This strengthens the case for the lift force variability being the result of the viscous drag force, i.e. the result of a reversible Stokes flow, not an inertial effect.

To further strengthen this case, the drag and lift forces in monolayers with $\sigma_1 = 0.06$ have also been studied as a function of the Reynolds number. Results in terms of force variability are shown in figure 15. The results clearly show that viscous scaling is appropriate for the drag as well as the lift force: r.m.s.(F_L)/$\mu\dot{\gamma}_b a^2$ becomes independent of Re for low values ($Re < 0.1$).
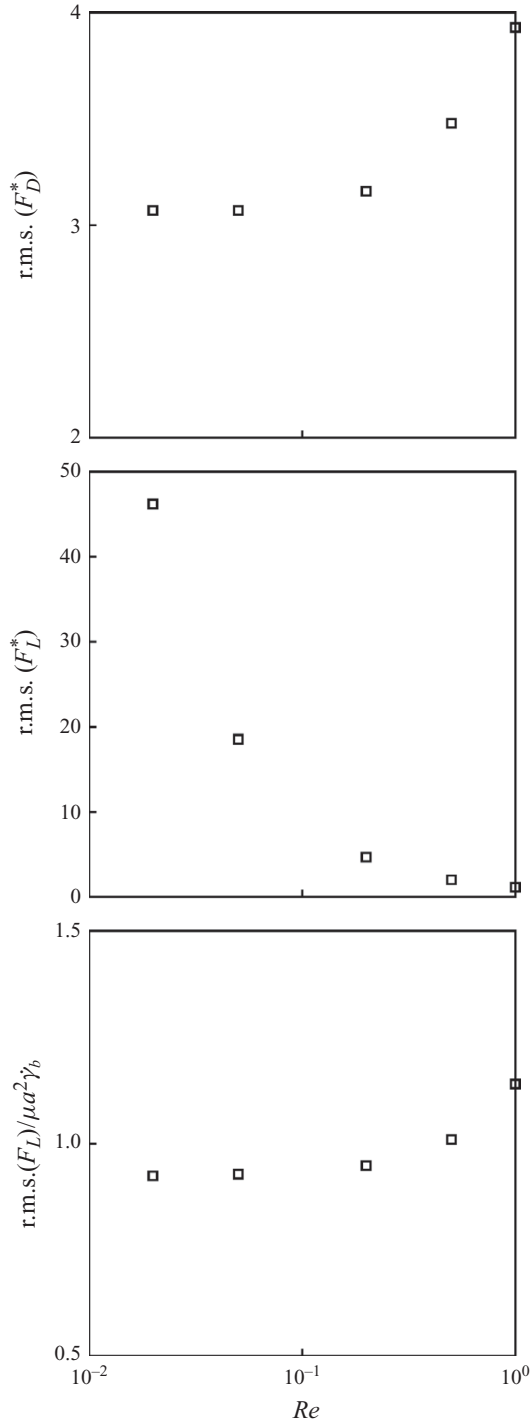
FIGURE 15. r.m.s.(F_D^*), r.m.s.(F_L^*) and r.m.s.$(F_L)/\mu a^2 \dot{\gamma}_b$ as a function of the Reynolds number for monolayers with $\sigma_1 = 0.06$ and $H = 12a$.
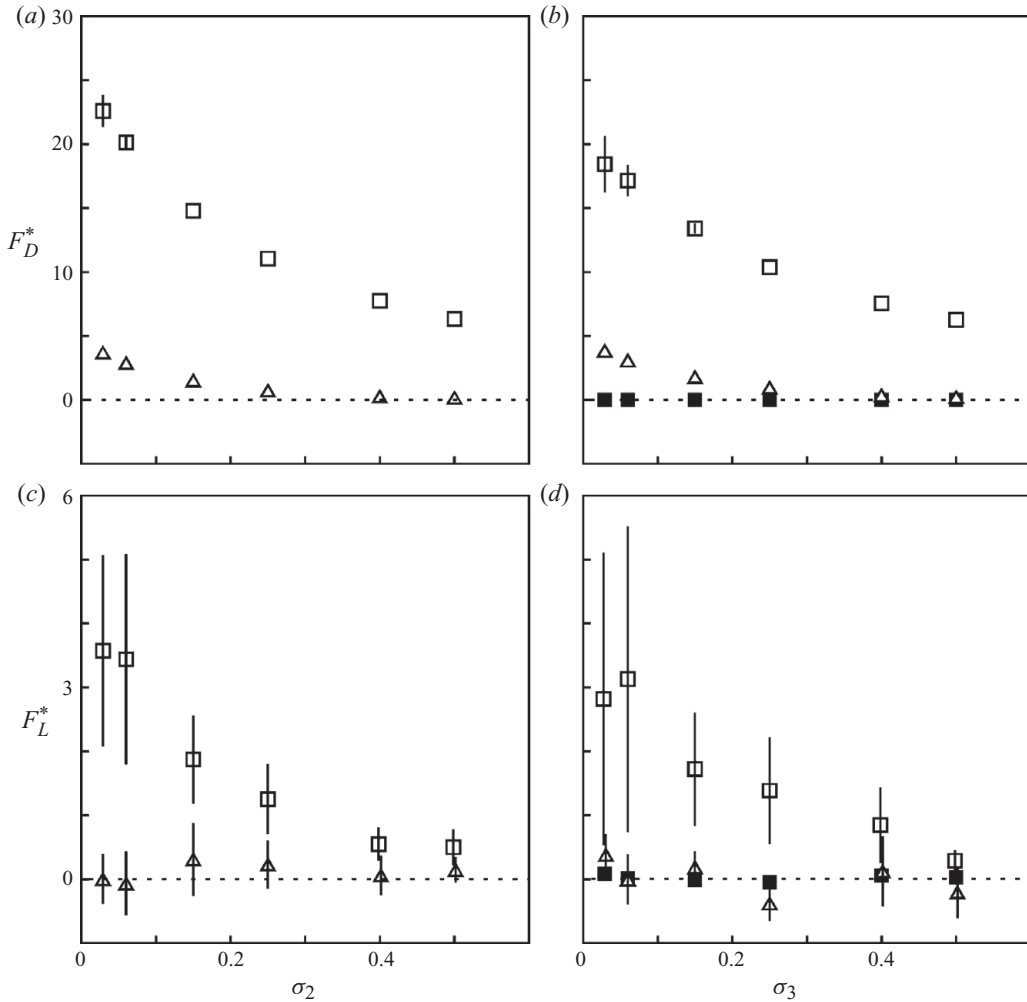
FIGURE 16. Dimensionless drag (*a,b*) and lift (*c,d*) forces as a function of the top-layer surface occupancy σ_2 for double layers (*a,c*) and σ_3 for triple layers (*b,d*). Open squares: top layer; triangles: second layer from the top; filled squares: third layer from the top. The total length of the error bars is two times the standard deviation. If the bars are smaller than the symbol, then they would not be displayed. For the sake of visibility of the error bars, some data points have been slightly shifted horizontally ($|\Delta\sigma| \leqslant 0.002$). $L = 48a$, $W = 32a$ and $Re = 0.05$. $H = 14a$ for double layers and $H = 16a$ for triple layers.

4.3. *Multiple layers*

We now briefly turn to double and triple layers of spheres, where we focus on how deep in the bed the shear flow is being felt and to what extent the average forces on spheres in the top layer depend on the underlying bed.

As was the case with monolayers, the average drag force on spheres in the top layer of double- and triple-layer beds decreases when the occupancy of the top layer increases (see figure 16*a,b*). The decay is less drastic than those for monolayers though. In beds made of double and triple layers the drag force on the spheres in the top layer at low σ is smaller than in monolayers at the same σ, and the drag force at high σ is larger than its monolayer counterpart.
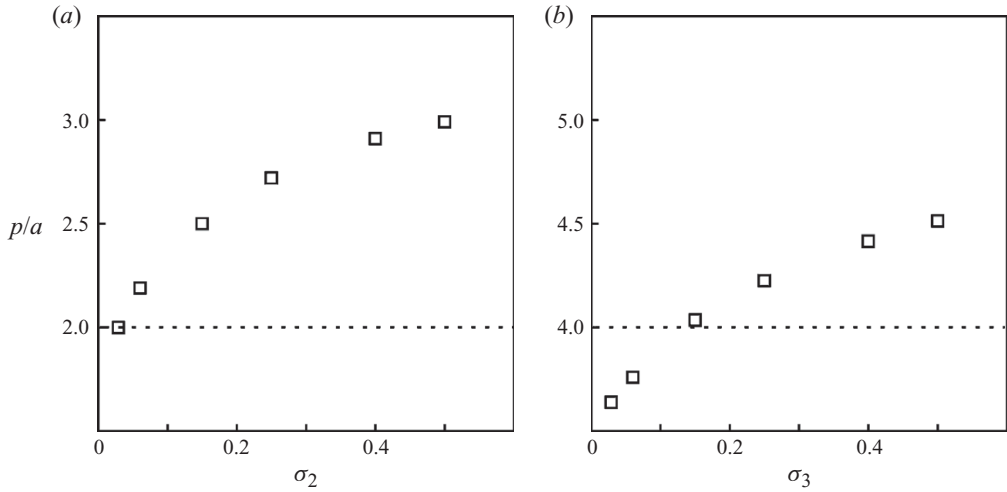
FIGURE 17. Intercept of the linear part of the velocity profile with the ordinate (symbol p) as a function of σ_2 for double layers (a) and σ_3 for triple layers (b). $L = 48a$, $W = 32a$ and $Re = 0.05$. $H = 14a$ for double layers and $H = 16a$ for triple layers. The dotted lines indicate the top of the layer underneath the highest layer.

These differences can be explained as follows. If we have multiple layers, the top spheres sink a little in the underlying bed which reduces the average drag force on the top-layer spheres. At the same time – due to the more open structure of the underlying bed – the shear flow is able to penetrate deeper into the top layer (see figure 17 and compare this with figure 11) which is an effect that enhances the drag force. The net effect is a weaker dependence of the average drag force on σ of the top layer. Average drag force on spheres in the second layer from the top is only appreciable for top-layer occupancies $\sigma_{2,3} < 0.2$; in the triple-layer bed the bottom layer hardly experiences an average drag force.

The results for the average lift force generally have large standard deviations of the averages (see figure $16c,d$); the top layer of the multiple-layer beds is more random than that of the monolayer beds (adding more layers increases the randomness). Compared to the drag force, the average lift force apparently is more sensitive to the specific placements of the spheres in the bed. It should be noted that the data points in figure 16 represent the averages of 5–7 (the latter for $\sigma_{2,3} \leqslant 0.06$) simulations with different (random) sphere configurations. The trends in the lift force, however, are the same as those for the drag force: reduced average forces at increasing top-layer surface occupancy, and low to negligible lift force levels in the lower sphere layers.

The increased randomness of the top layer in double- and triple-layer beds (also the z-centre location of the spheres now is a stochastic variable) compared to the monolayers makes the r.m.s. data somewhat less coherent, see figure 18. A few general observations can be made though. The deeper penetration of the shear flow along with the increased randomness of the top layer leads to (generally) larger r.m.s. values of the drag force and also to r.m.s.(F_D^*) being a less pronounced function of the top-layer occupancy, see figure 18(a,b). In monolayers, r.m.s.(F_D^*) quickly decreases with increasing σ_1 (beyond the maximum r.m.s.(F_D^*) that is reached at $\sigma_1 = 0.06$). This decrease is much less in double and triple layers. If we compare the drag r.m.s. data in relatively dense monolayers at $\sigma_1 = 0.5$ with the data for relatively dense top layers of double- and triple-layer beds ($\sigma_2 = 0.5$ and $\sigma_3 = 0.5$ respectively), we see two times and more than three times high r.m.s. levels of the drag force in the top
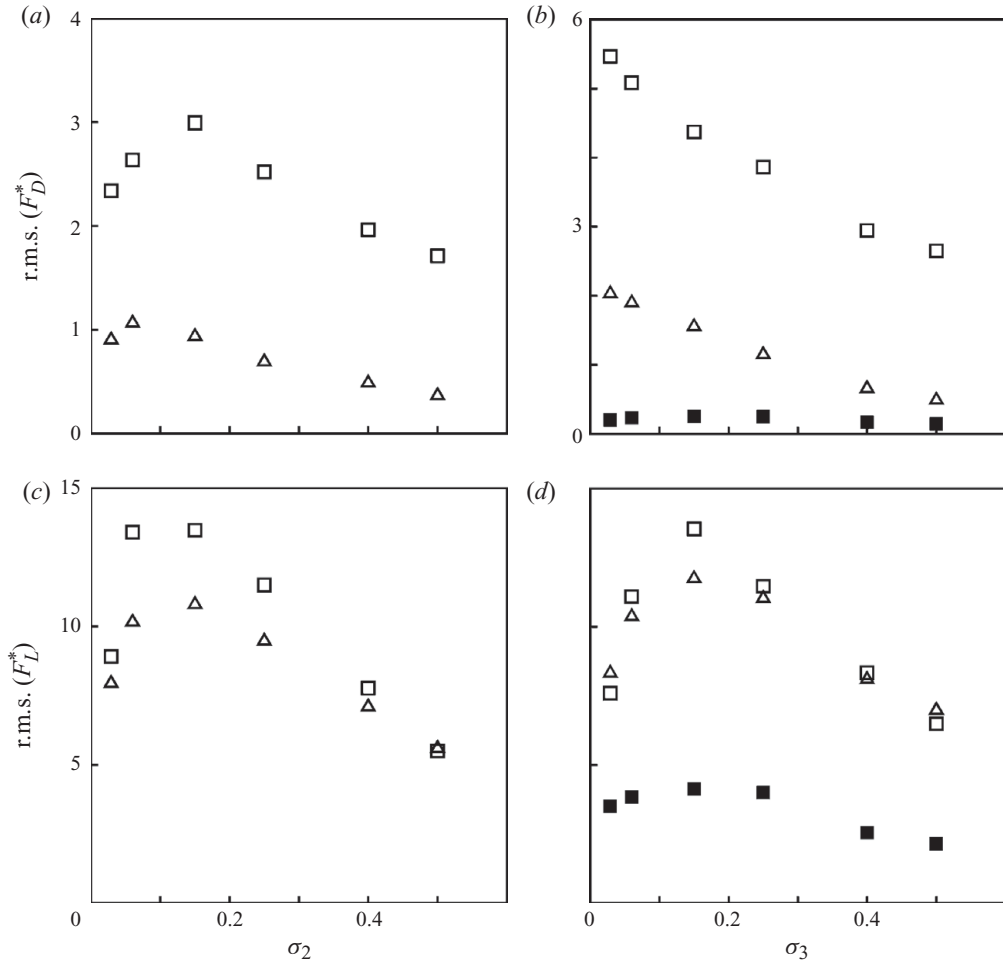
FIGURE 18. Root-mean-square values of the drag (*a,b*) and lift forces as a function of σ_2 for double layers (*a,c*) and σ_3 for triple layers (*b,d*). Open squares: top layer; triangles: second layer from the top; filled squares: third layer from the top. $L = 48a$, $W = 32a$ and $Re = 0.05$. $H = 14a$ for double layers and $H = 16a$ for triple layers.

layer of double- and triple-layer beds respectively compared to those of monolayer beds. Also, r.m.s.(F_D^*) takes on appreciable values for the second layer from the top, in double-layer as well as in triple-layer beds. This is because the subsequent layers in the bed communicate with one another via the interstitial fluid. At the low end of σ_2, the double-layer bed has a maximum r.m.s.(F_D^*) at $\sigma_2 = 0.15$. The triple layer r.m.s.(F_D^*) does not go through a maximum within the σ_3 range considered.

As in monolayers, r.m.s.(F_L^*) gets larger in double- and triple-layer beds than the single-sphere, dimensionless lift force of 9.22, see figure 18(*c,d*). The global trends in r.m.s.(F_L^*) in double- and triple-layer beds are similar to those in r.m.s.(F_D^*). The second layer from the top shows high r.m.s. lift force levels. They are comparable in size to the r.m.s. of the lift force in the top layer. This can be explained by considering the pressure distribution above and in the bed, as we do in figure 19. Spatial pressure fluctuations are largely due to the top-layer spheres. They are also very much felt by the spheres in the second (counted from the top) layer inducing net (mostly vertical) forces on these spheres, sometimes positive, sometimes negative, dependent on the
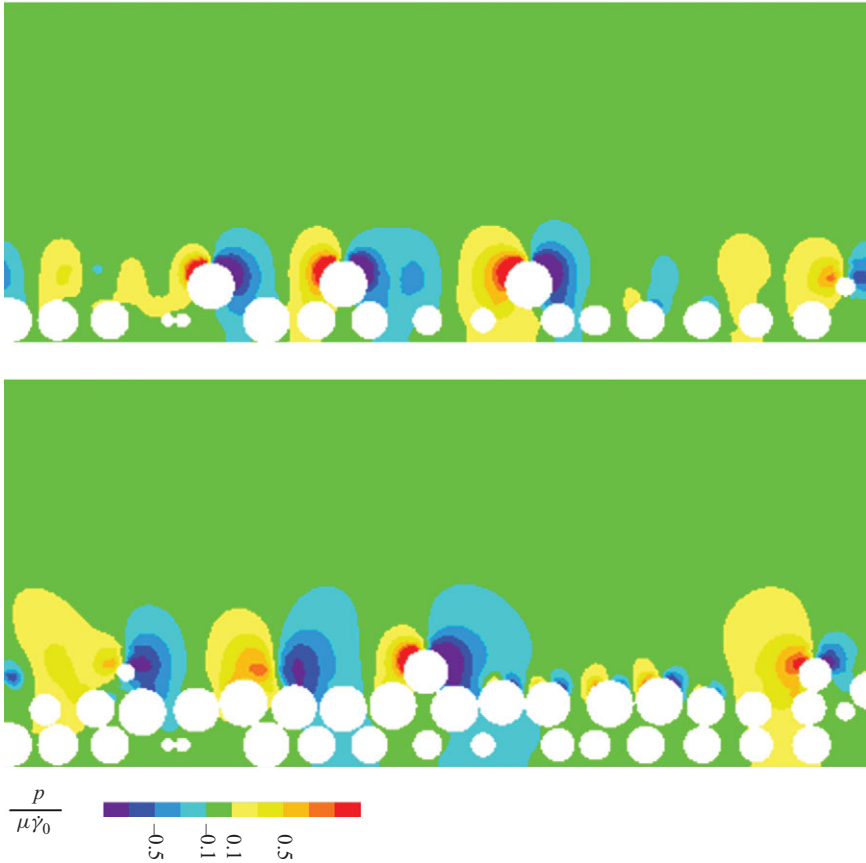
$$\frac{p}{\mu\dot{\gamma}_0}$$

FIGURE 19. Relative pressure contours in a vertical (xz) cross-section through (*a*) double-layer bed with $\sigma_2 = 0.25$, and (*b*) triple-layer bed with $\sigma_3 = 0.25$. $L = 48a$, $W = 32a$ and $Re = 0.05$. $H = 14a$ for double layer and $H = 16a$ for triple layer.

precise placement of the spheres above in the top layer. In the triple-layer system, the pressure fluctuations do hardly penetrate deeper than the middle layer of spheres so that the r.m.s. force levels (lift as well as drag) in the bottom layer are low (see figure 19*b* and 19*d*). Similar to the Stokes drag force on a single sphere, we have observed that the contributions due to normal stress and shear stress on the total force on individual spheres are (on average) roughly the same.

5. Summary and conclusions

Motivated by erosion of beds of fine particles as a result of fluid flow we studied the drag and lift forces on fixed, random assemblies of monosized spheres supported by a flat wall. The flow over the wall was a simple shear flow (driven by moving an opposing flat wall) with the Reynolds number based on the particle radius and the shear rate much smaller than 1 (in most simulations $Re = 0.05$). The research was based on directly solving the Navier–Stokes equations fully representing the geometry of the sphere assemblies. As a flow solver the LB method was used, and the spherical surfaces were represented with an immersed boundary method.

In order to assess the level of accuracy of the computational approach, numerical results were compared with the analytical solution for the drag and lift forces due to a shear flow on a sphere in contact with a flat wall (O'Neill 1968; Leighton & Acrivos

1985). This exercise showed that the drag force can be accurately represented by our numerical method (within 1 %). The lift force deviates by some 4 % and is mostly underestimated. The lift force shows the same dependence as the analytical solution (Leighton & Acrivos 1985) with respect to the Reynolds number if $Re \leqslant 0.01$. Under the flow conditions considered (Reynolds numbers much smaller than 1), the absolute value of the lift force is much smaller than the absolute value of the drag force.

The numerical procedure was also evaluated for flow systems involving multiple spheres. For one monolayer case (with surface occupancy of 0.25), it was shown that the drag and lift force results were within a few per cent independent of the computational grid. When studying the dependence of the drag and lift forces with respect to the wall-normal domain size, it was realized that the representative shear rate is the velocity gradient above the bed, not the apparent shear rate that follows from dividing the opposing wall velocity by the distance between the walls. The hydrodynamic forces for multiple sphere beds were all scaled using this representative shear rate.

The average drag and lift forces on spheres in a monolayer are pronounced monotonically decaying functions of the surface occupancy. The main effect responsible for this is the reduction of the penetration depth of the shear flow in the layer if its density increases. At the larger occupancies, the flow largely skims over the layer, which reduces drag to skin friction drag and which deteriorates the lift force. The sphere-to-sphere variability of the drag and the lift forces (as measured in terms of their r.m.s. levels) is significant. Both drag and lift r.m.s. levels have a maximum at surface occupancy 0.06. At $\sigma_1 = 0.06$ the r.m.s. of the drag force can get as high as 0.1 times the single-sphere drag force, whereas the r.m.s. of the lift force two times its single-sphere equivalent.

Point of discussion is whether this large force variability should be termed lift. The wall-normal forces on spheres in a monolayer are largely due to the hydrodynamic interactions of the spheres, inducing a hydrodynamic environment around spheres with significant wall-normal velocity components. The wall-normal flow is responsible for wall-normal hydrodynamic forces on the spheres that we term lift forces. These are reversible viscous forces (as opposed to inertial forces such as Saffman lift) as was confirmed by the viscous scaling of the wall-normal force variability as a function of the Reynolds number.

Next to monolayers of spheres, double and triple layers have been studied. All the double-layer simulations have the same (dense) ground layer on which randomly generated top layers are dropped. In the same manner all triple layers have the same two bottom layers and again randomly generated top layers. Given their topology, double- and triple-layer beds show more variability (in addition to the random wall-parallel sphere-centre positions, the wall-normal centre position of the upper layer(s) also varies to some extent). This makes it harder to generate statistically well-established average force data. A few trends can be discerned though. As compared to monolayers, the decay of the drag and lift forces with increasing surface coverage of the top layer – though still present – gets weaker. The drag and lift forces on top-layer spheres reduce as they prefer to sit in the lower places in between lower layer spheres and thus are less exposed to the shear flow. This effect is mostly felt in dilute top layers. The relative openness of multi-layer beds makes it easier for the shear flow to penetrate the top layer which (again in comparison to monolayers) enhances the drag and lift forces in beds with denser top layers. The combination of these two effects causes a levelling of the drag and lift forces in top layers of multiple-layer beds.

Average hydrodynamic forces quickly decay when going deeper in the bed. If the top layer has coverage greater than 0.2, the average drag and lift forces deeper in the

bed get insignificant. This is not the case for the r.m.s. force levels deeper in the bed. They are appreciable, at least in the second layer counted from the top.

Well-defined experiments on erosion of beds of spherical particles with narrow size distributions by laminar flow and the role of the Shields number have been reported by Charru, Mouilleron & Eiff (2004), Ouriemi *et al.* (2007) and Lobkovsky *et al.* (2008). The results of the simulations reported in this paper could be helpful in analysing the experimental results. In addition to the hydrodynamic forces acting on the spherical particles, such analysis would also require information regarding the topology of the bed, friction and restitution coefficients related to particle–particle collisions, and inter-particle forces in static beds and in beds in which particles move relative to one another (e.g. lubrication forces). With this in mind, we consider dynamic bed simulations. In principle, such simulations should reveal to what extent critical Shields numbers depend on bed and flow parameters, and how the topology of the bed and specifically its upper layers interact with the flow. It may be that spheres in upper layers align with the flow direction which would have impact on the drag and lift forces they experience.

A very interesting experimental study due to Charru *et al.* (2007) could serve as guidance and validation material on the route towards dynamic bed simulations. The study considers the motion of a single spherical particle over a bed of fixed particles as a result of a shear flow over the bed and highlights the role of the randomness of the underlying bed on the motion of the sphere.

REFERENCES

BEETSTRA, R., VAN DER HOEF, M. A. & KUIPERS, J. A. M. 2007 Drag force of intermediate Reynolds number flows past mono- and bidisperse arrays of spheres. *Am. Inst. Chem. Engrs J.* **53**, 489–501.

CHARRU, F., LARRIEU, E., DUPONT, J.-B. & ZENIT, F. 2007 Motion of a particle near a rough wall in a viscous shear flow. *J. Fluid Mech.* **570**, 431–453.

CHARRU, F., MOUILLERON, H. & EIFF, O. 2004 Erosion and deposition of particles on a bed sheared by a viscous flow. *J. Fluid Mech.* **519**, 55–80.

CHEN, S. & DOOLEN, G. D. 1998 Lattice-Boltzmann method for fluid flows. *Annu. Rev. Fluid Mech.* **30**, 329–364.

CHERAKUT, P. & MCLAUGHLIN, J. B. 1994 The inertial lift on a rigid sphere in a linear shear flow near a flat wall. *J. Fluid Mech.* **263**, 1–18.

CHERAKUT, P., MCLAUGHLIN, J. B. & DANDY, D. S. 1999 A computational study of the inertial lift on a sphere in a linear shear flow field. *Intl J. Multiphase Flow* **25**, 15–33.

COX, R. G. & HSU, S. K. 1977 The lateral migration of solid particles in a laminar flow near a plane. *Intl J. Multiphase Flow* **3**, 201–222.

DERKSEN, J. J. 2008 Flow-induced forces in sphere doublets. *J. Fluid Mech.* **608**, 337–356.

DERKSEN, J. J. 2009 Drag on random assemblies of spheres in shear-thinning and thixotropic liquids. *Phys. Fluids* **21**, 083302-1–9.

DERKSEN, J. J. & SUNDARESAN, S. 2007 Direct numerical simulations of dense suspensions: wave instabilities in liquid-fluidized beds. *J. Fluid Mech.* **587**, 303–336.

DERKSEN, J. & VAN DEN AKKER, H. E. A. 1999 Large-eddy simulations on the flow driven by a Rushton turbine. *Am. Inst. Chem. Engrs J.* **45**, 209–221.

DURU, P. & GUAZELLI, E. 2002 Experimental investigations on the secondary instability of liquid-fluidized beds and the formation of bubbles. *J. Fluid Mech.* **470**, 359–382.

DURU, P., NICOLAS, M., HINCH, J. & GUAZELLI, E. 2002 Constitutive laws in liquid-fluidized beds. *J. Fluid Mech.* **452**, 371–404.

EGGELS, J. G. M. & SOMERS, J. A. 1995 Numerical simulation of free convective flow using the lattice-Boltzmann scheme. *Intl J. Heat Fluid Flow* **16**, 357–364.

GOLDSTEIN, D., HANDLER, R. & SIROVICH, L. 1993 Modeling a no-slip flow boundary with an external force field. *J. Comput. Phys.* **105**, 354–366.

HASIMOTO, H. 1959 On the periodic fundamental solutions of the Stokes equations and their application to viscous flow past a cubic array of spheres. *J. Fluid Mech.* **5**, 317–328.

HILL, R. J., KOCH, D. L. & LADD, A. J. C. 2001 Moderate-Reynolds-number flows in ordered and random arrays of spheres. *J. Fluid Mech.* **448**, 243–278.

KANDHAI, D., DERKSEN, J. J. & VAN DEN AKKER, H. E. A. 2003 Interphase drag coefficients in gas-solid flows. *Am. Inst. Chem. Engrs J.* **49**, 1060–1065.

KING, M. R. & LEIGHTON, D. T. 1997 Measurement of the inertial lift on a moving sphere in contact with a plane wall in a shear flow. *Phys. Fluids* **9**, 1248–1255.

KRISHNAN, G. P. & LEIGHTON, D. T. 1995 Inertial lift on a moving sphere in contact with a plane in a shear flow. *Phys. Fluids* **7**, 2538–2545.

LADD, A. J. C. 1994 Numerical simulations of particle suspensions via a discretized Boltzmann equation. Part I. Theoretical foundation. *J. Fluid Mech.* **271**, 285–309.

LEIGHTON, D. & ACRIVOS, A. 1985 The lift on a sphere touching a plane wall in the presence of a simple shear flow. *J. Appl. Math. Phys. (Z. Angew. Math. Phys.)* **36**, 174–178.

LOBKOVSKY, A. E., ORPE, A. V., MOLLOY, R., KUDROLLI, A. & ROTHMAN, D. H. 2008 Erosion of a granular bed driven by laminar fluid flow. *J. Fluid Mech.* **605**, 47–58.

MCLAUGHLIN, J. B. 1993 The lift on a small sphere in wall-bounded linear shear flows. *J. Fluid Mech.* **246**, 249–265.

MOLLINGER, A. M. & NIEUWSTADT, F. T. M. 1996 Measurement of the lift force on a particle fixed to the wall in a viscous sublayer of a fully developed turbulent boundary layer. *J. Fluid Mech.* **116**, 285–306.

MOUILLERON, H., CHARRU, F. & EIFF, O. 2009 Inside the moving layer of a sheared granular bed. *J. Fluid Mech.* **628**, 229–239.

O'NEILL, M. E. 1968 A sphere in contact with a plane wall in a slow linear shear flow. *Chem. Engng Sci.* **23**, 1293–1298.

OURIEMI, M., AUSSILLOUS, P., MEDALE, M., PEYSSON, Y. & GUAZZELLI, E. 2007 Determination of the critical Shields number for particle erosion in laminar flow. *Phys. Fluids* **19**, 061706-1–4.

PATANKAR, N. A., HUANG, P. Y., KO, T. & JOSEPH, D. D. 2001a Lift-off of a single particle in Newtonian and viscoelastic fluids by direct numerical simulation. *J. Fluid Mech.* **438**, 67–100.

PATANKAR, N. A., KO, T., CHOI, H. G. & JOSEPH, D. D. 2001b A correlation for the lift-off of many particles in plane Poiseuille flows of Newtonian fluids. *J. Fluid Mech.* **445**, 55–76.

SAFFMAN, P. G. 1965 The lift on a small sphere in a slow shear flow. *J. Fluid Mech.* **22**, 385–400.

SAFFMAN, P. G. 1968 Correction. *J. Fluid Mech.* **31**, 624.

SANGANI, A. S. & ACRIVOS, A. 1982 Slow flow through a periodic array of spheres. *Intl J. Multiphase Flow* **8**, 343–360.

SOMERS, J. A. 1993 Direct simulation of fluid flow with cellular automata and the lattice-Boltzmann equation. *Appl. Sci. Res.* **51**, 127–133.

SUCCI, S. 2001 *The Lattice Boltzmann Equation for Fluid Dynamics and Beyond*. Clarendon.

TEN CATE, A., DERKSEN, J. J., PORTELA, L. M. & VAN DEN AKKER, H. E. A. 2004 Fully resolved simulations of colliding spheres in forced isotropic turbulence. *J. Fluid Mech.* **519**, 233–271.

TEN CATE, A., NIEUWSTAD, C. H., DERKSEN, J. J. & VAN DEN AKKER H. E. A. 2002 PIV experiments and lattice-Boltzmann simulations on a single sphere settling under gravity. *Phys. Fluids* **14**, 4012–4025.

VAN DER HOEF, M. A., BEETSTRA, R. & KUIPERS, J. A. M. 2005 Lattice-Boltzmann simulations of low-Reynolds-number flow past mono- and bidisperse arrays of spheres: results for the permeability and drag force. *J. Fluid Mech.* **528**, 233–254.

VASSEUR, P. & COX, R. G. 1976 The lateral migration of a spherical particle in two-dimensional shear flows. *J. Fluid Mech.* **78**, 385–413.

YIN, X. & SUNDARESAN, S. 2009 Drag law for bidisperse gas-solid suspensions containing equally sized spheres. *Ind. Engng Chem. Res.* **48**, 227–241.

ZENG, L., BALACHANDAR, S. & FISCHER P. 2005 Wall-induced forces on a rigid sphere at finite Reynolds number. *J. Fluid Mech.* **536**, 1–25.

ZENG, L., NAJJAR, F., BALACHANDAR, S. & FISCHER P. 2009 Forces on a finite-sized particle located close to a wall in a linear shear flow. *Phys. Fluids* **21**, 0333002-1–17.